Proceedings of FEDSM2007
5th Joint ASME/JSME Fluids Engineering Conference
July 30-August 2, 2007 San Diego, California USA

FEDSM2007-37189

ANALYSIS OF SOLID STRUCTURES AND STRESSES IN A GAS FLUIDIZED BED

Jin Sun*, and Francine Battaglia
Department of Mechanical Engineering
Iowa State University
Ames, Iowa 50011

ABSTRACT

Structures and stresses for the solid phase in a gas-solid fluidized bed are analyzed using results from hybrid simulations. The hybrid method couples the discrete element method (DEM) for particle dynamics with the averaged two-fluid (TF) equations for the gas phase. The coupling between the two phases is modeled using an interphase momentum transfer term. Structure information is characterized using force network size distribution, which shows no large force network existing in the fluidized bed. The normal contact forces have an exponentially decaying distribution. Solid phase continuum fields (local volume fraction, strain rate, stress tensor, and granular temperature) are computed using a coarse-graining process. The results show that the stress has difference in normal stress components. The collisional contribution is larger than the kinetic contribution and spatially correlated to force networks. Stresses are also computed using a kinetic theory stress model. It is demonstrated that the kinetic theory model predicts no difference in normal stress components and larger normal stresses than those computed from the coarse-graining process.

NOMENCLATURE

d	Particle diameter	(cm)
$\overline{\overline{D}}$	Strain rate tensor	$(1/\mathrm{s})$
e	Coefficient of normal restitution	
f	Scaled force magnitude	(dyne)
$\mathbf{F}$	Forces	(dyne)
$\mathbf{g}$	Acceleration of gravity	$(\mathrm{cm/s^2})$
I	Moment of inertia of a particle	$(\mathrm{g \cdot cm^2})$
$\mathbf{I}$	Interphase momentum transfer	$(\mathrm{dyne/cm^3})$
k	Stiffness coefficient of a particle	$(\mathrm{dyne/cm})$
m	Mass of a particle	(g)
n	Number density	
N	Particle number	
p	Pressure	$(\mathrm{dyne/cm^2})$
P	Probability density function	
$\mathbf{r}$	Position vector	(cm)
$\overline{\overline{S}}$	Gas stress tensor	$(\mathrm{dyne/cm^2})$
$\overline{\overline{T}}$	Solid stress tensor	$(\mathrm{dyne/cm^2})$
U	Fluidization velocity	$(\mathrm{cm/s})$
$\mathbf{u}$	Tangential displacement	(cm)
$\mathbf{v}$	Velocity for gas and solids	$(\mathrm{cm/s})$

Greek letters

β	Coefficient for drag forces	$(\mathrm{g/cm^3 \cdot s})$
δ	Normal compression in particle collision	(cm)
ε	Volume fraction	
μ_g	Gas shear viscosity	$(\mathrm{dyne \cdot s/cm^2})$
λ_g	Gas dilation viscosity	$(\mathrm{dyne \cdot s/cm^2})$
ω	Angular velocity	$(\mathrm{rad/s})$
ρ	Density	$(\mathrm{g/cm^3})$
θ	Translational granular temperature	$(\mathrm{cm^2/s^2})$

Superscripts/Subscripts

c	Collisional contribution to stresses
cell	Computational cell
coll	Collision
g	Gas phase
i	Index of a particle
k	Kinetic contribution to stresses

*Address all correspondence to this author: jinsun@iastate.edu.

n	Normal direction in the particle contact frame
t	Tangential direction in the particle contact frame
mf	Minimum fluidization
max	Maximum value
p	Particle
s	Solid

INTRODUCTION

Gas-solid fluidized beds are widely used in many industrial applications, e.g., fluid catalytic cracking, due to its good contacting between gas and solid phases, which prompts rapid heat and mass transfer and fast chemical reactions. However, the dynamics of gas-solid fluidized beds need to be better understood in order to improve existing processes and scale up new processes [1].

The dynamics of fluidized beds can be described at different levels of details [2]. At the most detailed level (atomic or molecular scale is not considered), the motion of the whole system is determined by the Newtonian equations of motion for the translation and rotation of each particle, and the fluid Navier-Stokes and continuity equations. The fluid motion and particle motion are linked by the no-slip condition on each particle boundary. At the second level, the fluid velocity at each point is replaced by its average. The Newtonian equations of motion are solved for each particle. The coupling force between fluid and particles is then related to the particle's velocity relative to the averaged fluid velocity, and to the local concentration of the particle assembly. At the third level, both the fluid velocity and the particle velocity are averaged to treat both gas and solid phases as interpenetrating continua. A description at this level is often referred to as the two fluid model (TFM). The TFM is able to describe large systems using much less computational resources than the methods at the other two levels. However, constitutive models must be postulated to account for the detailed motions lost in averaging. The constitutive modeling for solid phase stress is one of the most challenging tasks due to the complexity of granular flows [1].

Kinetic theory of granular flows (KTGF) has been successfully applied to the TFM for fluidization in the last decade [3]. The KTGF provides solid stress constitutive models for rapid granular flows of particles undergoing binary collision [4, 5]. However, a direct comparison of the stresses predicted by KTGF models with those in fluidized beds is not available since it is extremely difficult to experimentally measure the stress inside a fluidized bed. It remains unknown how well a KTGF constitutive model predicts the stress characteristics in fluidized beds.

The multiphase flows that comprise fluidized beds are intrinsically unstable, and spatial structures such as clusters and streamers of particles, and bubble-like voids are commonly observed [6]. It has been shown by our previous study [7] that multiple particle contacts exist in region away from bubbles in a fluidized bed. However, the structures were not quantified, thus their effect on stresses and the implication to the constitutive modeling are not clear.

In this paper, a hybrid model at the second level will be employed to address these questions. The hybrid model couples a TFM to solve fluid equations with a discrete element method (DEM) to solve the particle motion equations. Therefore, the hybrid model can simulate a fluidized bed at particle scales and produce useful information to analyze the structures as well as particle dynamics. From the particle information, solid continuum fields are then computed using a coarse-graining process. Solid stress characteristics can be analyzed and compared with a KTGF stress constitutive model.

The hybrid method is presented in the next section along with the method of computing solid continuum fields and the kinetic theory stress constitutive model. The computational specifications for a fluidized bed are described in the following section. Analysis and discussion of the results are then presented followed by the conclusions.

Simulation and analysis methods

Hybrid TF-DEM method

The hybrid method employs averaged equations for the gas phase, which are derived from the TFM. The governing equations for gas phase continuity and momentum balance, respectively, are [8]

$$\frac{\partial}{\partial t}(\varepsilon_{\mathrm{g}}\rho_{\mathrm{g}}) + \boldsymbol{\nabla}\cdot(\varepsilon_{\mathrm{g}}\rho_{\mathrm{g}}\mathbf{v}_{\mathrm{g}}) = 0 \quad , \tag{1}$$

and

$$\frac{\partial}{\partial t}(\varepsilon_{\mathrm{g}}\rho_{\mathrm{g}}\mathbf{v}_{\mathrm{g}}) + \boldsymbol{\nabla}\cdot(\varepsilon_{\mathrm{g}}\rho_{\mathrm{g}}\mathbf{v}_{\mathrm{g}}\mathbf{v}_{\mathrm{g}}) = \boldsymbol{\nabla}\cdot\overline{\overline{S}}_{\mathrm{g}} + \varepsilon_{\mathrm{g}}\rho_{\mathrm{g}}\mathbf{g} - \mathbf{I}_{\mathrm{gs}} \quad . \tag{2}$$

Particle dynamics is described by the Newtonian equations of motion. The discrete element method employs numerical integration of the motion equations to solve particle trajectories [9]. The translational and rotational motions of a particle for a fluidized bed are governed by

$$m_i\frac{\mathrm{d}\mathbf{v}_{\mathrm{p}i}}{\mathrm{d}t} = \mathbf{f}_{ci} + \mathbf{f}_{\mathrm{gp}i} + m_i\mathbf{g}, \tag{3}$$

$$I_i\frac{\mathrm{d}\boldsymbol{\omega}_i}{\mathrm{d}t} = \mathbf{T}_i, \tag{4}$$

where $\mathbf{f}_{ci}$ is the particle-particle contact force, $\mathbf{f}_{\mathrm{gp}i}$ is the fluid-particle interaction force, $m_i\mathbf{g}$ is the gravitational force, $\mathbf{T}_i$ is

the torque arising from the tangential components of the contact force, and I_i, $\mathbf{v}_{\mathrm{p}i}$, $\boldsymbol{\omega}_i$ are the moment of inertia, linear velocity and angular velocity, respectively. The net contact force, $\mathbf{f}_{\mathrm{c}i}$, and torque, $\mathbf{T}_i$, acting on each particle result from a vector summation of the force and torque at each particle-particle contact. A linear spring-dashpot model is employed for the contact force model due to its simplicity and reasonable accuracy [9]. Normal and tangential forces acting on particle i are calculated from the model as

$$\mathbf{F}_{\mathrm{n}_{ij}} = k_{\mathrm{n}}\delta_{ij}\mathbf{n}_{ij} - \gamma_{\mathrm{n}}m_{\mathrm{eff}}\mathbf{v}_{\mathrm{n}_{ij}}, \tag{5}$$

$$\mathbf{F}_{\mathrm{t}_{ij}} = -k_{\mathrm{t}}\mathbf{u}_{\mathrm{t}_{ij}} - \gamma_{\mathrm{t}}m_{\mathrm{eff}}\mathbf{v}_{\mathrm{t}_{ij}}, \tag{6}$$

where $k_{\mathrm{n,t}}$ and $\gamma_{\mathrm{n,t}}$ are the spring stiffness and viscoelastic constants, respectively, and $m_{\mathrm{eff}} = m_i m_j/(m_i + m_j)$ is the effective mass of spheres with masses m_i and m_j. The corresponding contact force on particle j is simply given by Newton's third law, i.e., $\mathbf{F}_{ji} = -\mathbf{F}_{ij}$. The total contact force and torque acting on particle i are then given by

$$\mathbf{f}_{\mathrm{c}i} = \sum_j (\mathbf{F}_{\mathrm{n}ij} + \mathbf{F}_{\mathrm{t}ij}), \tag{7}$$

$$\mathbf{T}_i = -\frac{1}{2}\sum_j \mathbf{r}_{ij} \times \mathbf{F}_{\mathrm{t}ij}, \tag{8}$$

where $\mathbf{r}_{ij}$ is the vector connecting center of particle j to the center of particle i.

The coupling term between the equations for gas and particle motion is the gas-particle interaction $\mathbf{I}_{\mathrm{gs}}$ in the gas momentum equation and $\mathbf{f}_{\mathrm{gp}i}$ in the particle equation of motion. The fluid-particle interaction force per unit volume of bed, $\mathbf{I}_{\mathrm{gs}}$, in the gas momentum equation is the sum of the gas forces, $\mathbf{f}_{\mathrm{gp}i}$, over all the particles in a fluid cell and dividing by the volume of the fluid cell, V_{cell}. Thus

$$\begin{aligned}\mathbf{I}_{\mathrm{gs}} =& \frac{\sum_i^{N_{\mathrm{cell}}} \mathbf{f}_{\mathrm{gp}i}}{V_{\mathrm{cell}}} \\ =& -\varepsilon_{\mathrm{s}}\boldsymbol{\nabla}p_{\mathrm{g}} + \varepsilon_{\mathrm{s}}\boldsymbol{\nabla}\cdot\overline{\overline{\tau}}_{\mathrm{g}} + \sum_i^N \varepsilon_{\mathrm{g}}\mathbf{f}_{\mathrm{d}i}/V_{\mathrm{cell}},\end{aligned} \tag{9}$$

where N_{cell} is the number of particles in a fluid cell [10]. The last term in Eq. (9) is calculated approximately using local mean gas and particle velocities

$$\sum_i^N \varepsilon_{\mathrm{g}}\mathbf{f}_{\mathrm{d}i}/V_{\mathrm{cell}} = \beta(\mathbf{v}_{\mathrm{g}} - \mathbf{v}_{\mathrm{s}}), \tag{10}$$

where β is calculated using the correlations developed by Ergun [11], and Wen and Yu [12],

$$\beta = \begin{cases} 150\frac{\varepsilon_{\mathrm{s}}^2}{\varepsilon_{\mathrm{g}}d_{\mathrm{p}}^2}\mu_{\mathrm{g}} + 1.75\varepsilon_{\mathrm{s}}\frac{\rho_{\mathrm{g}}}{d_{\mathrm{p}}}|\mathbf{v}_{\mathrm{g}} - \mathbf{v}_{\mathrm{s}}| & \text{for } \varepsilon_{\mathrm{g}} \le 0.8 \\ \frac{3}{4}C_{\mathrm{D}}\frac{\varepsilon_{\mathrm{g}}\varepsilon_{\mathrm{s}}}{d_{\mathrm{p}}}\rho_{\mathrm{g}}|\mathbf{v}_{\mathrm{g}} - \mathbf{v}_{\mathrm{s}}|\varepsilon_{\mathrm{g}}^{-2.7} & \text{for } \varepsilon_{\mathrm{g}} > 0.8. \end{cases} \tag{11}$$

This mean drag force is then assigned back to each particle in the cell to obtain $\mathbf{f}_{\mathrm{gp}i}$ according to the particle volume.

A Fortran code, Multiphase Flow with Interphase eXchanges (MFIX), is used for all simulations in this work. MFIX uses a finite volume approach with a staggered grid for the discretization of the TFM governing equations to reduce numerical instabilities [13]. Scalars such as pressure and volume fraction are stored at the cell centers and the velocity components are stored at cell surfaces. A second-order discretization is used for spatial derivatives and first-order discretization for temporal derivatives. A modified SIMPLE algorithm is employed to solve the discretized equations [13]. The explicit time integration method is used to solve the translational and rotational motion equations used in the DEM [9, 14]. The readers are referred to reference [7] for a more detailed account of the hybrid method.

Computation of solid continuum fields

The solid continuum fields are computed using a coarse-graining process. The coarse-graining operator is defined as

$$< \varphi >_{\mathrm{CG}} (\mathbf{r}) = \sum_i^N G(\mathbf{r} - \mathbf{r}_i)\varphi_i, \tag{12}$$

where i is the index of a particle, N is the number of particles in the system, φ is a property of particle i, $\mathbf{r}$ is the position of the continuum field, and $\mathbf{r}_i$ is the center of mass of particle i. The coarse-graining function, $G(\mathbf{R})$, is a positive semi-definite normalized function [15]. The coarse-graining function used in this paper is

$$G(\mathbf{R}) = \frac{1}{V_{\mathrm{w}}}\mathcal{H}(\mathbf{W} - \mathbf{R}), \tag{13}$$

where $\mathbf{W}$ is the width vector of the coarse-graining function, $\mathcal{H}(\mathbf{W} - \mathbf{R}) = H(W_x - R_x)H(W_y - R_y)H(W_z - R_z)$ with H

being the Heaviside function, and $V_{\rm w} = W_x W_y W_z$, in a three-dimensional Cartesian system.

To improve statistical accuracy, an ensemble of independent samples is required in the spirit of ensemble averaging. The ensemble averaging can be approximately achieved by time averaging as described in [16], which is used in this paper. The samples are just the particle configurations at independent time instances. The time interval should be large enough to avoid the correlation between the samples. Defining M to be the number of samples, then the coarse-graining operation shown in Eq. 12 is re-defined as

$$< \varphi >_{\rm CG} (\mathbf{r}) = \frac{1}{M} \sum_j^M \left(\sum_i^N G(\mathbf{r} - \mathbf{r}_i) \varphi_i \right)_j . \quad (14)$$

The number density n (solid volume fraction $\varepsilon_{\rm s} = n \frac{\pi}{6} d_{\rm p}^3$) is computed using $\varphi = 1$ in Eq. 14 as

$$n(\mathbf{r}) =< 1 >_{\rm CG} (\mathbf{r}). \quad (15)$$

The averaging operator is defined as

$$< \varphi > (\mathbf{r}) = \frac{1}{n(\mathbf{r})} < \varphi >_{\rm CG} (\mathbf{r}). \quad (16)$$

The hydrodynamic velocity $\mathbf{v}_{\rm s}(\mathbf{r})$ is then defined as

$$\mathbf{v}_{\rm s}(\mathbf{r}) =< \mathbf{v}_{\rm p} > , \quad (17)$$

where $\mathbf{v}_{\rm p}$ is the particle velocity. The solid strain rate tensor is defined as

$$\overline{\overline{D}} = \frac{1}{2} \left[\boldsymbol{\nabla} \mathbf{v_s} + (\boldsymbol{\nabla} \mathbf{v_s})^{\rm T} \right], \quad (18)$$

where $(\boldsymbol{\nabla} \mathbf{v_s})^{\rm T}$ is the transpose of the velocity gradient. The translational granular temperature is defined as

$$\begin{aligned} \theta =& \frac{1}{\mathcal{D}} < \mathbf{C} \cdot \mathbf{C} > \\ =& \frac{1}{\mathcal{D}} {\rm tr}(< \mathbf{v}_{\rm p} \mathbf{v}_{\rm p} > - < \mathbf{v}_{\rm p} >< \mathbf{v}_{\rm p} >), \end{aligned} \quad (19)$$

where $\mathbf{C} = \mathbf{v}_{\rm p} - \mathbf{v}_{\rm s}$ is the particle fluctuation velocity, ${\rm tr}()$ is the trace of a tensor, and $\mathcal{D}$ is the dimensionality of the system. (The word "translational" is omitted hereafter since only translational granular temperature is used in this paper.)

The stress have two contributions. The first is the kinetic (or dynamic) stress due to momentum flux transported by particle fluctuations. The second is the collisional (or viral) stress due to particle contacts. The stress tensor is defined as

$$\overline{\overline{T}} = \overline{\overline{T}}^k + \overline{\overline{T}}^c. \quad (20)$$

The kinetic contribution is

$$\overline{\overline{T}}^k =< m \mathbf{C} \mathbf{C} >_{\rm CG} , \quad (21)$$

and the collisional contribution is

$$\overline{\overline{T}}^c =< \sum_{j, j \neq i}^N \frac{1}{2} \mathbf{r}_{ij} \mathbf{F}_{ij} >_{\rm CG} , \quad (22)$$

where$\mathbf{F}_{ij}$ is the contact force acting on particle i by particle j.

Kinetic theory constitutive model

A solid stress constitutive model is given by kinetic theory (KT) for granular flows for smooth, slightly inelastic particles [5]

$$\overline{\overline{T}}^{KT} = \overline{\overline{T}}^{KTk} + \overline{\overline{T}}^{KTc}, \quad (23)$$

where $\overline{\overline{T}}^{KTk}$ is the kinetic contribution

$$\begin{aligned} \overline{\overline{T}}^{KTk} =& \rho_s \varepsilon_{\rm s} \theta \overline{\overline{I}} - \frac{2\mu}{\eta(2-\eta) g_0} \\ & \left[1 + \frac{8}{5} \eta (3\eta - 2) \varepsilon_{\rm s} g_0 \right] (\overline{\overline{D}} - \frac{1}{3} {\rm tr}(D) \overline{\overline{I}}), \end{aligned} \quad (24)$$

and $\overline{\overline{T}}^{KTc}$ is the collision contribution

$$\begin{aligned} \overline{\overline{T}}^{KTc} =& 4 \rho_s \varepsilon_{\rm s}^2 \eta g_0 \theta \overline{\overline{I}} - \frac{16 \mu \varepsilon_{\rm s}}{5(2-\eta)} \\ & \left[1 + \frac{8}{5} \eta (3\eta - 2) \varepsilon_{\rm s} g_0 \right] (\overline{\overline{D}} - \frac{1}{3} {\rm tr}(D) \overline{\overline{I}}) \\ & - \frac{256}{5\pi} \eta \mu \varepsilon_{\rm s}^2 g_0 \left[\frac{3}{5} (2 \overline{\overline{D}} + {\rm tr}(D) \overline{\overline{I}}) \right]. \end{aligned} \quad (25)$$

In Eqs. 24 and 25, $\eta = \frac{1}{2}(1+e)$, $\mu = 5m(\theta/\pi)^{1/2}/16 d_{\rm p}^2$, ${\rm tr}(D)$ is the trace of the strain rate tensor $\overline{\overline{D}}$ and g_0 is the radial distribution function for particles. The Carnahan-Starling formula [17] $g_0 = (2 - \varepsilon_{\rm s})/2(1 - \varepsilon_{\rm s})^3$ is used in this paper.

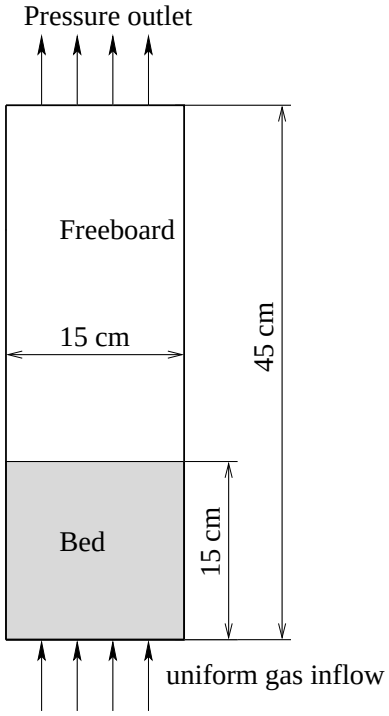

Figure 1. SCHEMATIC SHOWING COMPUTATIONAL DOMAIN FOR THE GOLDSCHMIDT ET AL. [18] EXPERIMENT.

Table 1. COMPUTATIONAL PARAMETERS AND GENERAL INITIAL AND BOUNDARY CONDITIONS

Geometry:	
Width of domain, x	15 cm
Height of domain, y	45 cm
Horizontal grid size, Δx	1 cm
vertical grid size, Δy	1 cm
Particle properties:	
Particle diameter	0.25 cm
Particle density	2.526 g/cm^3
Particle stiffness coefficient	8×10^5 dyne/cm
Particle damping coefficient	1.77 dyne $\cdot$ s/cm
Particle normal restitution coefficient	0.97
Particle friction coefficient	0.1
Initial conditions:	
ε_{g}	1.0
$v_{\mathrm{g}}(= U_{\mathrm{mf}})$	128 cm/s
Initial bed height	15 cm
Particle number	4000
Boundary conditions:	
Air inlet velocity	$1.5U_{\mathrm{mf}}$ cm/s
Specified pressure at outlet	101325 Pa
Wall boundary for gas phase	No slip
Particle wall interaction:	
Wall stiffness coefficient	1.2×10^6 dyne/cm
Wall damping coefficient	3.93 dyne $\cdot$ s/cm

COMPUTATIONAL CASE

A gas-solid fluidized bed is simulated using the hybrid TFDEM model presented in the methodology subsection. The simulation for a bubbling fluidized bed with a uniform air inflow is performed. The simulation is based on the experiment of the bubbling fluidized bed by Goldschmidt et al. [18]. The fluidized beds simulated have very small depths compared to the other two dimensions. Therefore, simulations are performed using one layer of spherical particles in the third dimension. The simulation is designed to mimic the same experiment conditions. The computational domain is shown in Fig. 1 and the computational parameters are shown in table 1.

The case is computed for 20 seconds of simulation time. Particle configuration samples are taken after 5 seconds to minimize the start-up effect on the finite sampling time period since the system reaches a dynamically quasi-steady state [19] at that time. The time interval for sampling is 0.1 second.

RESULTS AND DISCUSSION

The hybrid simulation of fluidized bed dynamics for the case has been validated in a previous study [7]. The study showed that the hybrid method predicts the bed dynamics with reasonable agreement with experimental and TFM results. The current study focuses on the analysis of solid phase structures and stresses using the particle information provided by the hybrid simulations.

Particles form a force network by interacting with their neighbors via contact forces. Force networks are the structures of interest in this paper. Force networks have a very prominent effect on how momentum is transfered in granular media [20,21]. If a large force network spanning the whole granular media exists, the momentum is mainly transferred by the enduring contacts between particles. If binary contacts or single particles dominate instead of a large force network, the momentum is transferred mainly by particle fluctuations and collisions. The

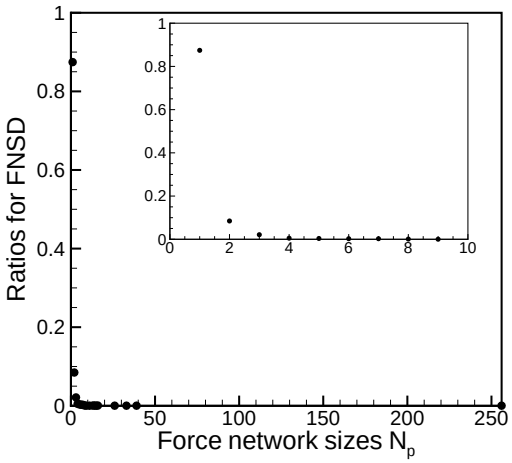

Figure 2. FORCE NETWORK SIZE DISTRIBUTION AT TIME OF 5 S. THE SIZE IS QUANTIFIED BY THE NUMBER OF PARTICLES IN A FORCE NETWORK. THE INSET SHOWS THE CLOSE-UP VIEW OF THE SIZE DISTRIBUTION OF FORCE NETWORKS WITH 1-10 PARTICLES.

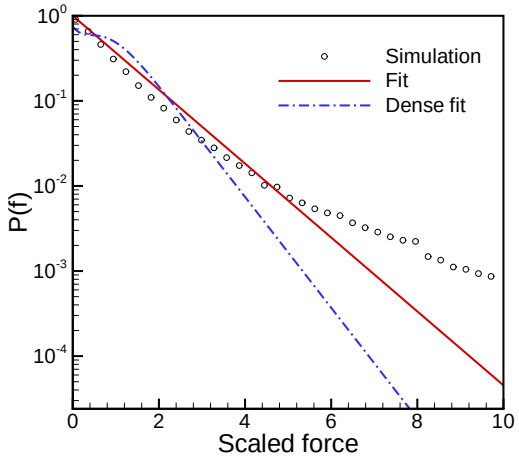

Figure 3. PROBABILITY DENSITY FUNCTION OF NORMAL CONTACT FORCES. THE SOLID LINE INDICATES THE EXPONENTIAL FIT, $P(f) = \exp(f)$. THE DASH-DOT LINE INDICATES THE FIT FOR DENSE GRANULAR MEDIA, $P(f) = a(1 - be^{-f^2})e^{-\beta f}$ WITH $a = 3.0, b = 0.75$, AND $\beta = 1.5$.

size of force network is simply quantified by the number of particles N_p in a force network in this paper. A single particle is deemed as a limiting case of a force network. The force network size distribution (FNSD) is characterized by the ratio of the number of the force networks with N_p particles to the total number of force networks. The instantaneous FNSD at 5 seconds is shown in Fig. 2. It can be seen that 90% of the force networks only consist of a single particle, i.e., $N_\mathrm{p} = 1$ (refer to the inset in Fig. 2). The second probable force networks are formed by binary particle collisions. The largest force network has about 250 particles with a very low ratio. The distributions at other time instances have very similar trends and are not shown here. The distribution shown in Fig. 2 is direct proof that there is no large force network spanning the whole fluidized bed with the fluidization velocity of $1.5U_\mathrm{mf}$. The constitutive behavior is then expected to be dominated by particle free-flight motions and collisions instead of multiple contacts.

The normal contact force distribution is shown in Fig. 3, in which the probability density P is plotted as a function of magnitudes of normal contact forces, f, scaled by the average force. The normal contact force distribution follows an exponential decay, comparable to an exponential fit of $P(f) = \exp(f)$ as indicated by the solid line in Fig. 3. This distribution shares the exponential decay feature present in granular packing [22, 23] and dense granular flows [21], where large force networks exist, but differs in that the plateau for small forces is lacking. A fit function for force distributions in dense granular media is also plotted for comparison purposes. The fit function is of the form $P(f) = a(1-be^{-f^2})e^{-\beta f}$ with $a = 3.0$, $b = 0.75$, and $\beta = 1.5$. The well-spread distribution indicates the contact forces in the fluidized bed are heterogeneous, i.e., some particle experience small forces while others experience much larger forces. The exponential decay implies a higher probability of finding large compared to a Gaussian distribution, which is proved to be a robust feature of granular media [24]. Lack of the plateau indicates that small forces are less populated than those in dense granular media, which distinguishes the contact force distribution in fluidized beds.

To manifest the spatial correlation between force networks and solid stresses, an instantaneous particle configuration at a time of 5 seconds is studied. The particle positions are shown by dots in Fig. 4(a) and the number of contacting neighbors (N_c[1]) to a particle are denoted by contour levels in the figure. The multiple contacts ($N_\mathrm{c} > 1$) show the locations of force networks (including binary collisions). The solid phase continuum fields are obtained using the coarse-graining process of Eq. 14. The width of the coarse-graining function is set to $W_x = 1\,\mathrm{cm}$, $W_y = 1\,\mathrm{cm}$ and $W_z = d_\mathrm{p} = 0.25\,\mathrm{cm}$. The number of samples is one in this case, i.e., $M = 1$. The collisional stress components, T^c_{xx}, T^c_{yy} and T^c_{xy}, are shown in Figs. 4(b), 4(c) and 4(d), respectively. The solid volume fractions are shown in Fig. 4(e). The high volume fractions correspond to the high N_c region. The kinetic stress components, T^k_{xx}, T^k_{yy} and T^k_{xy}, are shown in Figs. 4(f), 4(g) and

[1] N_c varies between 0 and 6 in this case since 6 is the maximum possible number of contacting neighbors in a two-dimensional configuration of identical spheres.

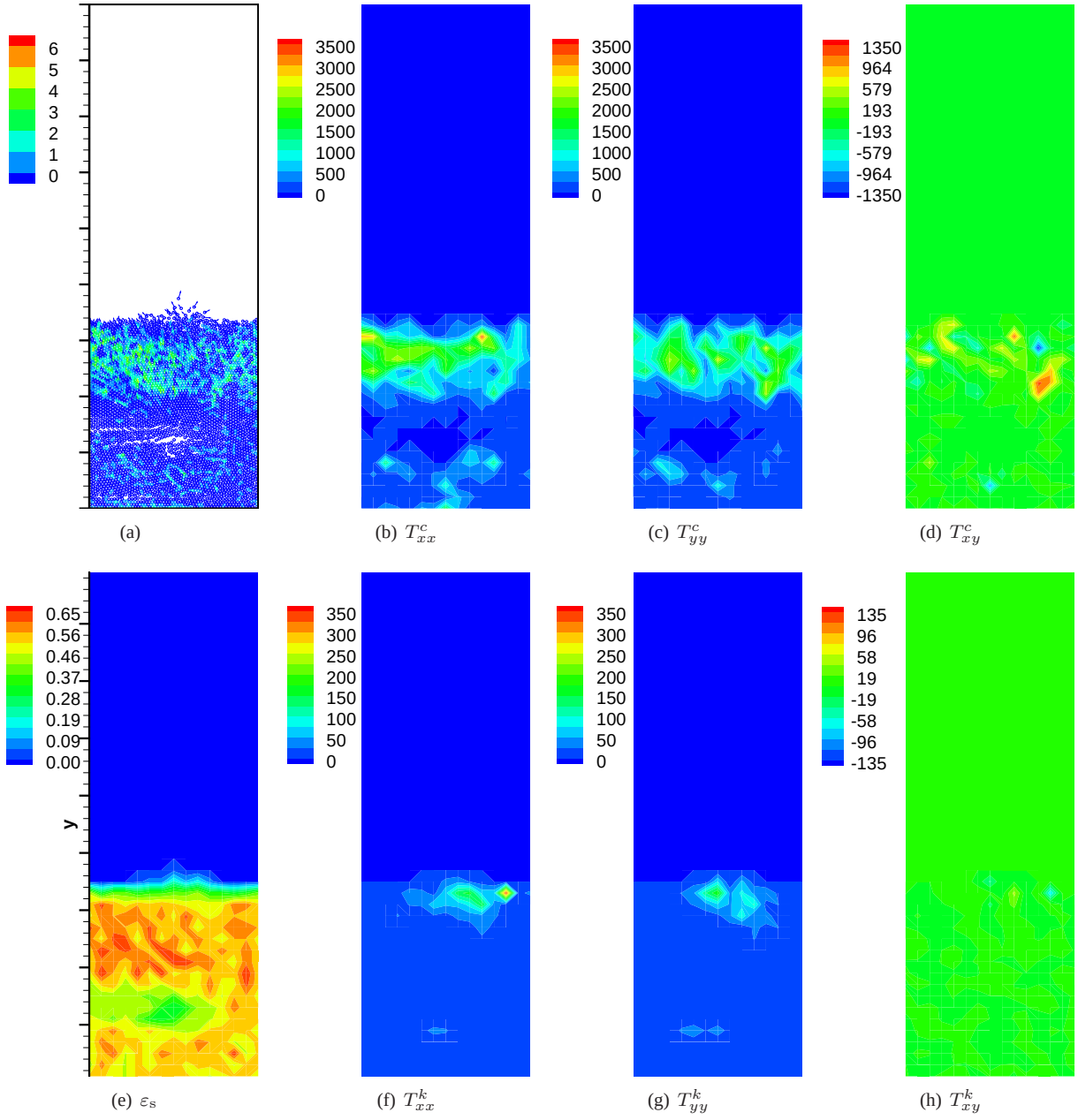

Figure 4. INSTANTANEOUS PARTICLE CONFIGURATION, SOLID VOLUME FRACTIONS AND STRESS COMPONENTS AT 5 SECOND. PARTICLE POSITIONS ARE SHOWN AS POINTS AND THE N_c NUMBERS ARE SHOWN BY CONTOUR LEVELS IN (a). THE COLLISIONAL STRESS COMPONENTS ARE SHOWN IN (b) T^c_{xx}, (c) T^c_{yy} AND (d) T^c_{xy}. SOLID VOLUME FRACTIONS ARE SHOWN IN (e). THE KINETIC STRESS COMPONENTS ARE SHOWN IN (f) T^k_{xx}, (g) T^k_{yy} AND (h) T^k_{xy}. THE UNIT OF STRESSES IS $\mathrm{dyne/cm^2}$.

4(h), respectively. The collisional stresses are the dominant contributions to the total stresses; about ten (10) times larger than the kinetic stresses. The locations of large collisional stresses are positively correlated to the locations of force networks. For example, comparing Figs. 4(a)–4(d), both large collisional stresses and force networks occur in the upper region above the bubble. The locations of kinetic stresses, however, are not directly correlated to the force networks, but to the high velocity region near the free surface. Thus, force networks locations provide information as to location of the collisional stresses. This confirms that the findings of force networks (multiple contacts) [7] are useful for investigating fluidized bed constitutive behaviors.

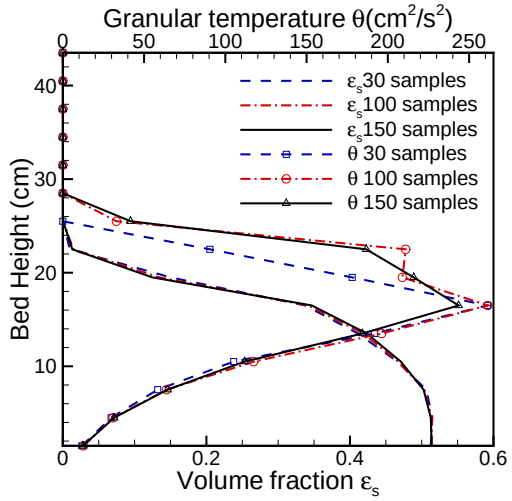

Figure 5. SOLID VOLUME FRACTIONS AND GRANULAR TEMPERATURES AS FUNCTIONS OF BED HEIGHTS. RESULTS FROM $M = 30$, $M = 100$ AND $M = 150$ ARE COMPARED.

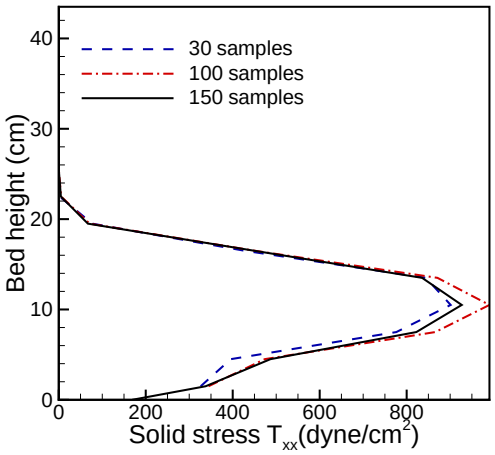

Figure 6. SOLID STRESS COMPONENT T_{xx} AS A FUNCTION OF BED HEIGHTS. RESULTS FROM $M = 30$, $M = 100$ AND $M = 150$ ARE COMPARED.

The detailed characteristics of stresses at a quasi-steady state are investigated using results obtained from multiple samples, i.e., $M > 1$. The width of the coarse-graining function is set to $W_x = 15\,\mathrm{cm}$, $W_y = 3\,\mathrm{cm}$ and $W_z = d_\mathrm{p} = 0.25\,\mathrm{cm}$. In this way, the field variables are obtained as univariate functions of the bed height. The statistical effect of number of samples, M, on the continuum fields obtained by the coarse-graining process is investigated. The solid volume fraction ε_s and granular temperature θ obtained from coarse-graining processes with $M = 30$, $M = 100$ and $M = 150$ are plotted in Fig. 5 as functions of bed heights. It can be seen that the volume fraction has little variation with respect to sampling, as shown with the three cases. The granular temperature has noticeable differences for sampling with $M = 30$ and the other two sampling cases in the dilute bed region, where volume fraction is less than 0.3 and bed height is higher than 16 cm. The difference is caused by the greater velocity fluctuations due to less particles in the dilute region. However, the granular temperature calculated using $M = 100$ and $M = 150$ are reasonably close. Thus, the continuum fields are statistically converging with regard to the sample sizes. The same convergence is observed for the solid stress component T_{xx} shown in Fig. 6 (the other components of the stress tensor have the same behavior and are not plotted to avoid cluttering the figure). The continuum fields obtained from $M = 150$ using coarse-graining process are presented in the following discussion for the small statistical error in this case.

The normal stresses, T_{xx} and T_{yy}, and the shear stress T_{xy}, are computed across the bed width ($W_x = 15\,\mathrm{cm}$) and shown in relation to the bed height in Figs. 7(a), 7(b) and 7(c), respectively, for their kinetic (superscript k) and collisional (superscript c) contributions. Note that the shear stress T_{yx} is similar to T_{xy} and is not shown. The kinetic contributions of the normal stresses T^k_{xx} and T^k_{yy} demonstrate that these stresses increase with increasing bed height, reaching a maximum at 16 cm, which is the height of the bed expansion (i.e., the interface between the dense and dilute flow regimes), and then rapidly decrease in dilute region. The shear stress kinetic contribution T^k_{xy} exhibits positive stresses in the dense bed and negative stresses in the dilute region (greater than 16 cm). Another observation is that the kinetic normal stress T^k_{yy} in the streamwise direction (y–direction) is greater than T^k_{xx} because the particles fluctuate more vigorously in the streamwise direction. The collisional contributions of the normal and shear stresses, however, peak at a bed height of 10 cm, where the collisions are most prevalent. The collisional contribution T^c_{yy} is also greater than T^k_{xx} in the streamwise direction affected by the same fluctuation difference in different directions. This observation is consistent to the normal stress difference observed in simple shear flows of granular materials [25, 26]. Overall, the collisional contributions are greater than the kinetic contributions for both the normal and shear stresses, demonstrating that particle collisions dominate the stress behavior.

The kinetic theory constitutive stress model presented in Eqs. 24 and 25 is tested by substituting for the solid volume fractions, granular temperatures and strain rates computed from the coarse-graining process. The strain rates are calculated using a central-difference numerical scheme. The normal stresses T^{KT}_{xx} and T^{KT}_{yy}, and the shear stress T^{KT}_{xy} are also shown in Figs. 7(a)–7(c), respectively. The kinetic theory model predicts almost the same normal stresses, i.e., for the kinetic contributions, $T^{KTk}_{xx} \approx T^{KTk}_{yy}$ and for the collisional contributions,

$T_{xx}^{KTc} \approx T_{yy}^{KTc}$. Thus, the kinetic theory models presented in Eqs. 24 and 25 is not capable of capturing the normal stress difference present in the fluidized bed. A kinetic theory model using the Burnett correction [27] may be necessary to correctly capture this feature of the stresses in the fluidized beds. Since the kinetic theory stresses are calculated using the same particle velocity fluctuations as the coarse-graining process, it can be shown that $T_{xx}^{KTk} = T_{yy}^{KTk} = (T_{xx}^{k} + T_{yy}^{k} + T_{zz}^{k})/\mathcal{D}$, which can be verified by comparing Eq. 21 with Eq. 24. Compared to the stresses obtained directly using coarse-graining, the collisional normal stresses predicted by kinetic theory model agree well at the dense region (bed height is lower than 6 cm), but are over-predicted at the dilute region. This over-prediction is partially due to the higher granular temperature at the dilute region (see Fig. 5). The shear stresses predicted by the kinetic theory model do not agree well with the coarse-grained stresses. The over-prediction of normal stresses and disagreements of shear stresses indicate more investigations on the constitutive model is necessary.

CONCLUSIONS

A gas-solid fluidized bed has been simulated using a hybrid TF-DEM method. Detailed analyses of the solid phase structures and stresses have been performed. The force network size distribution shows that a large force network does not exist under a fluidization velocity of $1.5U_{\mathrm{mf}}$. Particle normal contact forces have an exponentially decaying distribution , which indicates the heterogeneity of the contact forces. Lack of a plateau for small forces is a distinct feature of the distribution compared to that for dense granular media. The solid stresses have differences in the normal stress components. The collisional contribution to the solid stress is found to be larger than the kinetic contribution and spatially correlated to force networks. The kinetic theory stress model predicted no difference in normal stress components and over-predicted the collision contributions to the normal stresses. The analyses have demonstrated the characteristics of structures and stresses in a typical fluidized bed at a well-fluidized state. The comparisons to the kinetic theory constitutive model probe the inability of the model and point out the potential need for a Burnett order constitutive model for fluidized bed modeling.

The analysis methods demonstrated in this paper can be applied to a large range of fluidization states. The results will reveal the constitutive behavior of fluidized beds under different fluidization conditions and may also provide directions for constitutive modeling.

REFERENCES

[1] Sundaresan, S., 2000. "Modeling the hydrodynamics of multiphase flow reactors: Current status and challenges". AIChE Journal, **46** (6) , pp. 1102–1105.

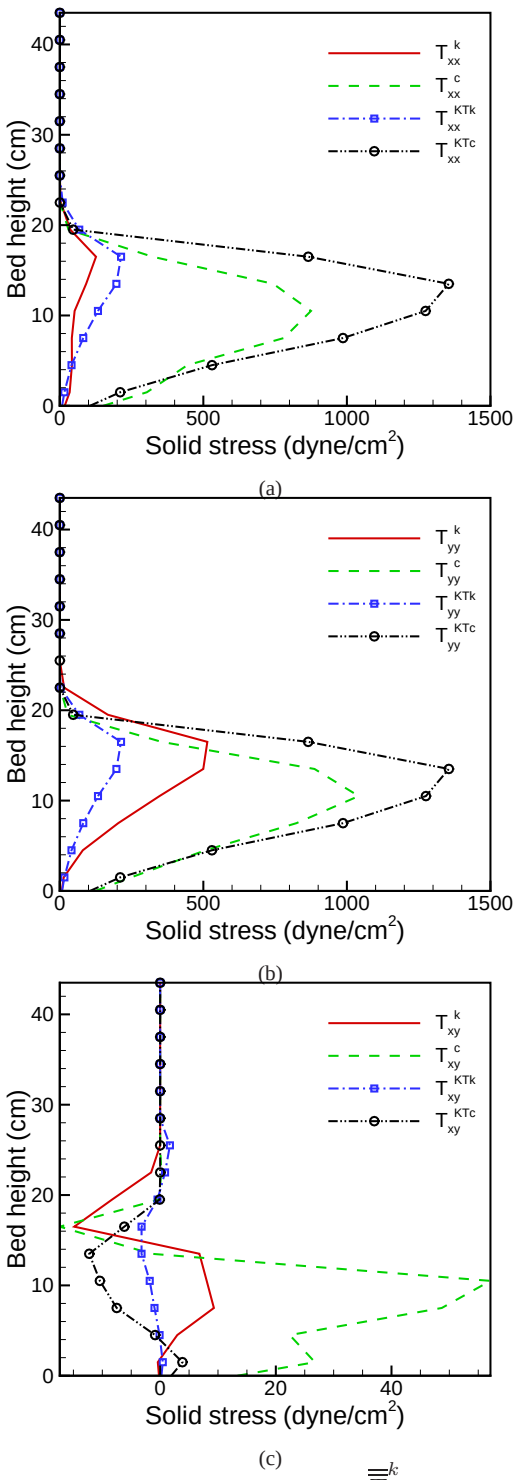

Figure 7. THE KINETIC CONTRIBUTION, $\overline{\overline{T}}^{k}$, AND COLLISIONAL CONTRIBUTION, $\overline{\overline{T}}^{c}$, TO THE SOLID STRESS ARE COMPARED. THE xx, yy AND xy COMPONENTS ARE SHOWN IN SUB-FIGURES (a), (b) AND (c), RESPECTIVELY. THE CORRESPONDING COMPONENTS PREDICTED BY KINETIC THEORY MODEL, $\overline{\overline{T}}^{KTk}$ AND $\overline{\overline{T}}^{KTc}$, ARE ALSO SHOWN ACCORDINGLY.

[2] Jackson, R., 2000. *The Dynamics of Fluidized Particles*. Cambridge University Press.

[3] Gidaspow, D., Jung, J., and K., S. R., 2004. "Hydrodynamics of fluidization using kinetic theory: an emerging paradigm 2002 flour-daniel lecture". *Powder Technology*, **148** , pp. 123–141.

[4] Jenkins, J., and Savage, S., 1983. "A theory for the rapid flow of identical, smooth, nearly elastic, spherical particles". *Journal of Fluid Mechanics*, **130** , pp. 187–202.

[5] Lun, C. K., Savage, S. B., Jeffrey, D. J., and Chepurniy, N., 1984. "Kinetic theories for granular flow: Inelastic particles in couette flow and slightly inelastic particles in a general flow field". *Journal of Fluid Mechanics*, **140** , pp. 223–256.

[6] Gidaspow, D., 1994. *Multiphase flow and fluidization: Continuum and kinetic theory descriptions*. Academic Press, Boston, USA.

[7] Sun, J., Battaglia, F., and Subramaniam, S., 2006. "Hybrid two-fluid dem simulation of gas-solid fluidized beds". In American Society of Mechanical Engineers, Fluids Engineering Division (Publication) FED, vol. 262, pp. IMECE2006–14831.

[8] Syamlal, M., Rogers, W., and O'Brien, T., 1993. MFIX documentation: Theory guide. Technical Note DOE/METC-95/1013, NTIS/DE95000031, National Energy Technology Laboratory, Department of Energy. See also URL `http://www.mfix.org`.

[9] Cundall, P. A., and Strack, D. L., 1979. "A discrete numerical model for granular assemblies". *Gèotechnique*, **29** , pp. 47–65.

[10] Anderson, T. B., and Jackson, R., 1967. "A fluid mechanical description of fluidised beds". *Industrial and Engineering Chemistry Fundamental*, **6** , pp. 527–539.

[11] Ergun, S., 1952. "Fluid flow through packed columns". *Chemical Engineering Progress*, **48** , pp. 89–94.

[12] Wen, C. Y., and Yu, Y. H., 1966. "Mechanics of fluidization". In *Fluid particle technology*, vol. 62 of *Chemical Engineering Progress Symposium Series*. American institute of chemical engineers, pp. 100 –111.

[13] Syamlal, M., 1998. MFIX documentation: Numerical technique. Technical Note DOE/MC31346-5824, NTIS/DE98002029, National Energy Technology Laboratory, Department of Energy. See also URL `http://www.mfix.org`.

[14] Hoomans, B. P., Kuipers, J. A., Briels, W. J., and van Swaaij, W. P., 1996. "Discrete particle simulation of bubble ans slug formation in a two-dimensional gas-fluidised bed: A hard-sphere approach". Chemical Engineering Science, **51** (1) , pp. 99–118.

[15] Goldenberg, C., Atman, A. P. F., Claudin, P., Combe, G., and Goldhirsch, I., 2006. "Scale separation in granular packings: Stress plateaus and fluctuations". *Physical Review Letters*, **96** , pp. 168001–4.

[16] Allen, M. P., and Tildesley, D. J., 1987. *Computer simulation of liquids*. Clarendon Press, Oxford.

[17] Carnahan, N. F., and Starling, K. E., 1969. "Equation of state for nonattracting rigid spheres". Journal of Chemical Physics, **51** (2) July , pp. 635–636.

[18] Goldschmidt, M. J., Link, J. M., Mellema, S., and Kuipers, J. A., 2003. "Digital image analysis measurements of bed expansion and segregation dynamics in dense gas-fluidised beds". *Powder Technol.*, **138** , pp. 135–159.

[19] Sun, J., and Battaglia, F., 2006. "Hydrodynamic modeling of particle rotation for segregation in bubbling gas-fluidized beds". Chemical Engineering Science, **61** (5) , pp. 1470 – 1479.

[20] Campbell, C. S., 2002. "Granular shear flows at the elastic limit". *Journal of Fluid Mechanics*, **465** , pp. 261–291.

[21] Sun, J., Battaglia, F., and Subramaniam, S., 2006. "Dynamics and structures of segregation in a dense, vibrating granular bed". Physical Review E (Statistical, Nonlinear, and Soft Matter Physics), **74** (6) , pp. 061307–13.

[22] Mueth, D. M., Jaeger, H. M., and Nagel, S. R., 1998. "Force distribution in a granular medium". Physical Review E, **57** (3) March , pp. 3164–3169.

[23] Silbert, L. E., Grest, G. S., and Landry, J. W., 2002. "Statistics of the contact network in frictional and frictionless granular packings". Physical Review E (Statistical, Nonlinear, and Soft Matter Physics), **66** (6) , p. 061303.

[24] Silbert, L. E., 2006. "Force heterogeneities in particle assemblies: From order to disorder". Physical Review E (Statistical, Nonlinear, and Soft Matter Physics), **74** (5) , pp. 051303–7.

[25] Campbell, C. S., and Gong, A., 1986. "The stress tensor in a two dimensional granular shear flow". *Journal of Fluid Mechanics*, **164** , pp. 107–125.

[26] Walton, O. R., and Braun, R. L., 1986. "Stress calculations for assemblies of inelastic spheres in uniform shear". *Acta Mechanica*, **63** , pp. 73–86.

[27] Goldhirsch, I., and Sela, N., 1996. "Origin of normal stress differences in rapid granular flows". Phys. Rev. E, **54** (4) Oct , pp. 4458–4461.